coatings

MDPI

Article

Effects of Composition-Tuned Ni–Ti Catalytic Coatings on Wear and Corrosion Resistance of Gas-Nitrided Q420 Steel

Hongyong Shao, Junming Li *, Mingtao Chen and Xiaocui Lv

School of Mechanical and Automotive Engineering, Guangxi University of Science and Technology, Liuzhou 545006, China; 20240102019@stdmail.gxust.edu.cn (H.S.); 20250101056@stdmail.gxust.edu.cn (M.C.); 20250101010@stdmail.gxust.edu.cn (X.L.)
* Correspondence: jmli@gxust.edu.cn

Abstract

Q420 steel is widely used in steel bridge connection components; however, wear and corrosion during service can significantly compromise its service life. Gas nitriding can improve the mechanical properties of Q420 steel, but its conventional implementation is characterized by low nitriding efficiency. In this study, Ni–Ti coatings with Ni/(Ni + Ti) atomic ratios ranging from 54.1% to 82.4% were deposited on Q420 steel by dual-target magnetron sputtering to serve as catalytic layers, followed by gas nitriding at 500 °C for 6 h. The results demonstrate that Ni–Ti coatings significantly promote nitriding, while the nitrided layer thickness exhibits a non-monotonic dependence on Ni content. The sample containing 70.4 at.% Ni exhibited the maximum effective nitrided layer thickness of 8.87 μm, approximately 2.25 times that of the directly nitrided counterpart. The sample containing 54.1 at.% Ni achieved the highest surface hardness of 843.24 HV, representing increases of 24.9% and 319.9% relative to the directly nitrided and untreated Q420 steel, respectively. Meanwhile, the sample containing 70.4 at.% Ni exhibited a corrosion current density I_{corr} of 0.191 mA·cm^{-2}, corresponding to reductions of 51.0% and 27.7% relative to the untreated and directly nitrided samples, respectively. EDS and XRD analyses of the nitrided samples revealed pronounced changes in the elemental distribution and phase composition of the surface layers, indicating that the Ni–Ti catalytic coating participated in and modified the microstructural evolution during nitriding. The observed performance improvements can be primarily attributed to the ability of the Ni–Ti surface layer to promote NH_3 dissociation and facilitate the diffusion of reactive nitrogen species.

Keywords: Q420 steel; Ni–Ti coatings; gas nitriding; wear resistance; corrosion resistance

1. Introduction

Steel bridges are essential components of transportation infrastructure, spanning highways, railways, and cross-sea transport links, whose structural performance directly influences the safety and service life of the broader transportation network [1,2]. As a high-strength structural steel, Q420 combines ultrahigh strength, excellent toughness, favorable hardenability, and superior fatigue resistance, making it the core specialized material for heavy-duty steel bridges [3]. However, under sustained traffic loading and complex environmental conditions, critical load-bearing and connecting components of steel bridges are susceptible to corrosion, fatigue damage, and contact wear, which can compromise their load-bearing capacity, structural integrity, and long-term service safety [4,5]. In addition to the substantial maintenance costs associated with corrosion and wear, tribological interactions in mechanical systems account for approximately 23% of global primary energy

Check for updates

Received: 22 October 2026
Revised: 12 November 2026
Accepted: 12 November 2026
Published: 17 November 2026

Copyright: © 2026 by the authors. Licensee MDPI, Basel, Switzerland. This article is an open access article distributed under the terms and conditions of the Creative Commons Attribution (CC BY) license.

consumption, while friction-related losses in the transportation sector represent approximately 30% of its total energy consumption [6,7]. Accordingly, enhancing the corrosion and wear resistance of critical steel bridge components is essential for preserving structural integrity, ensuring long-term operational safety, and minimizing energy losses [8].

Thanks to its core advantages—including the metallurgical bonding interface, controllable hard-facing layer thickness, and excellent thermal stability—thermochemical hardening technology has become the preferred solution for surface hardening of steel components [9–11]. Gas nitriding can significantly enhance surface hardness, wear resistance, and corrosion resistance while largely preserving the toughness of the underlying substrate [12,13]. Previous studies have examined the effects of nitriding temperature and holding time on the microstructure and wear resistance of nitrided layers, as well as the use of staged and two-step nitriding processes to tailor their microstructural characteristics and mechanical properties [14,15]. These studies demonstrate that optimizing key process parameters, including nitriding temperature, duration, and atmosphere, enables effective regulation of the phase composition, microstructural morphology, and hardness distribution of nitrided layers.

To improve nitriding efficiency, increasing research attention has been directed toward coating-assisted catalytic nitriding. Previous studies have demonstrated that depositing rare-earth-containing coatings on steel surfaces can promote the formation of thicker nitrided layers within shorter treatment times [16]. Yan et al. [17] reported that the incorporation of rare-earth elements enhances nitrogen uptake at the substrate surface and facilitates subsequent nitrogen transfer and diffusion into the substrate. Subsequent investigations further confirmed the catalytic effects of rare-earth elements during nitriding. Extensive studies by Yan et al. have demonstrated the beneficial catalytic effects of rare-earth elements during the nitriding and nitrocarburizing of various steels, including stainless steels [18,19] and alloy steels [20,21]. Furthermore, nickel (Ni)-based coatings are also attractive and cost-effective surface-engineering materials, and numerous studies have demonstrated that Ni can substantially improve the corrosion and oxidation resistance of steels [22–24]. The pivotal role of Ni in catalyzing nitriding has also been widely recognized [25,26]. Studies have shown that Ni atoms in solid solution can facilitate nitrogen diffusion and accelerate nitride precipitation [27,28]. Combining first-principles calculations with experimental validation, Chen et al. [29] demonstrated that Ni doping reduced the energy barrier for nitrogen penetration from the surface into the substrate from 1.80 to 1.57 eV, and that for diffusion along octahedral interstitial sites from 0.72 to 0.44 eV. Experimentally, Ni microalloying increased the compound layer thickness by 62.0% and the surface hardness by 47.9%. Furthermore, Ni–Ti alloying can synergistically enhance the mechanical properties and corrosion resistance of coatings, with previous studies demonstrating that Ti–Ni films exhibit excellent wear resistance, high hardness, and favorable corrosion resistance [30,31]. Margono et al. [32] nitrided Ti–Ni films and reported a corrosion rate of only 3.64×10^{-4} mm/year and a minimum corrosion current density of 2.80×10^{-4} A/cm^2, which were attributed to the formation of a stable passive film. Plasma nitriding increased the surface hardness of these Ti–Ni films to 392.4 HV, while treatment with a dual-phase Ti–Ni film increased the surface hardness of the Al 6061 substrate from 101.2 to 663.9 HV and reduced its wear rate by 87%. Other studies have employed Ni-based catalytic coatings for gas nitriding of pure iron and 304 stainless steel, aiming to achieve efficient low-temperature nitriding while avoiding the formation of brittle layers associated with conventional gas nitriding. These studies establish the feasibility of Ni-based coating-assisted steel nitriding; however, their substrates have predominantly been pure iron or austenitic stainless steel, with neither compositional regulation of bimetallic Ni–Ti coatings nor the potential wear- and corrosion-resistant functionality of the coatings after nitriding being investigated.

Nevertheless, previous studies have either focused on the nitriding behavior of coatings themselves to improve the surface hardness, wear resistance, and corrosion resistance of alloys [33], or employed monometallic Ni-based coatings, rare-earth coatings, or Ni microalloying to catalyze steel nitriding. Studies on depositing Ni–Ti coatings onto low-alloy steels such as Q420 and exploiting their compositional tunability to regulate the nitriding kinetics of the steel substrate remain scarce. Moreover, conventional catalytic coatings are generally regarded as sacrificial media during nitriding and do not inherently provide wear or corrosion resistance, whereas directly deposited functional coatings may impede nitrogen diffusion owing to their dense microstructures [34]. The proposed coating architecture requires the coating to perform two simultaneous roles during nitriding: serving as a transport pathway for reactive nitrogen species and subsequently transforming in situ into a wear- and corrosion-resistant surface layer [35]. However, these two functions have predominantly been addressed separately in previous studies, with catalytic layers facilitating nitrogen ingress and functional layers providing wear and corrosion resistance during service [36]. Nevertheless, a systematic criterion for determining the optimal Ni/Ti ratio that balances the catalytic nitrogen-transport capability with the subsequent mechanical functionality of the coating remains lacking.

Based on the above considerations, this study proposes depositing a Ni–Ti coating with both catalytic activity and mechanical functionality onto the surface of Q420 steel, in which Ni promotes the dissociation of reactive nitrogen species while Ti accelerates nitrogen diffusion into the substrate during nitriding. Following nitriding, the coating is expected to transform in situ into wear- and corrosion-resistant layers containing phases such as TiN and Ti_2N, forming a continuous graded structure with the underlying nitrided layer and thereby avoiding the detrimental effects of conventional alloying on substrate properties. The Ti fraction was selected as the primary compositional variable to prepare Ni–Ti coatings with different Ni/Ti ratios. Through systematic microstructural and phase characterization, hardness measurements, tribological testing, and electrochemical analyses, this study examines the influence of Ti fraction on nitriding behavior and the microstructural evolution of the nitrided layer. The mechanisms underlying the improved wear and corrosion resistance associated with the coating–nitrided-layer architecture are further explored, with particular attention to the potential contributions of its compositional and microstructural gradients. This study offers a potential strategy for integrating coating-assisted nitriding with surface strengthening while preserving the bulk composition of Q420 steel, providing a basis for the gradient surface engineering of critical steel bridge components.

2. Experimental Procedure and Methods

2.1. Substrate Material and Sample Preparation

The material used in this study was commercially available Q420 (Yiheng Steel Trading Co., Ltd., Wuyang, China) low-alloy high-strength structural steel. For subsequent experiments, the steel substrate was sectioned into 25 mm × 25 mm × 8 mm block specimens using wire electrical discharge machining. To minimize machining-induced residual stresses and surface deformation, the specimens were annealed at 600 °C for 1 h. The metallographic microstructure and X-ray diffraction (XRD, Rigaku Corporation, Tokyo, Japan) pattern of the annealed Q420 steel are shown in Figure 1, revealing a predominantly body-centered cubic (BCC) α-Fe ferritic structure. The chemical composition of the steel was determined using an optical emission spectrometer (Jiaxinhai Machinery Equipment Co., Ltd., Tianjin, China), and the results are presented in Table 1. Before the experiments, the specimens were mechanically polished and subsequently polished using a velvet polishing cloth with 2.5 μm abrasive paste (Meixiang Instrument Sales Department, Wuhan, China). All specimens

were ultrasonically cleaned in ethanol before testing to remove residual abrasive particles and surface contaminants.

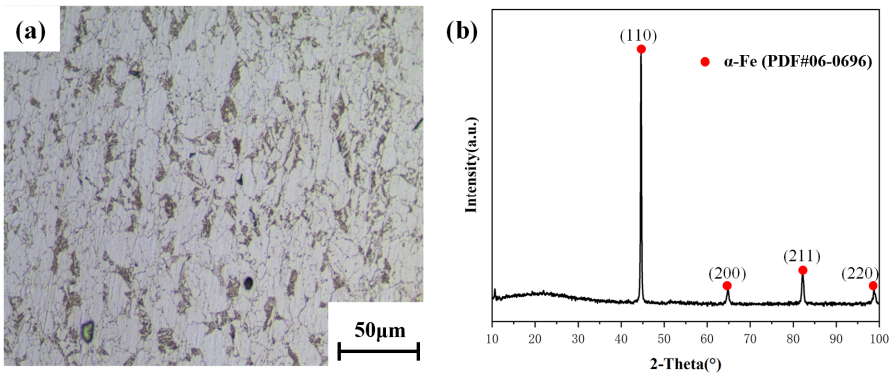


Figure 1. (**a**) Optical micrograph of the annealed Q420 steel; (**b**) XRD pattern of the annealed Q420 steel.

Table 1. Chemical composition of Q420 steel (wt%).

Element	C	Si	Mn	Mo	S	Cr	Nb	Ti	Fe
wt.%	0.09	0.28	1.54	0.01	0.028	0.19	0.036	0.016	Balance

Ni–Ti coatings were deposited onto Q420 steel substrates using a magnetron sputtering system (Truth Equipment Co., LTD, Hefei, China), as schematically illustrated in Figure 2a. The coatings were fabricated by co-sputtering Ti and Ni targets, both with a purity of 99.99%, a diameter of 50 mm, and a thickness of 5 mm. The target-to-substrate distance was fixed at 17 cm, with the targets positioned at an angle of 25° relative to the substrate surface. Prior to sputtering, the chamber was evacuated to a base pressure of 5.0×10^{-4} Pa using a mechanical pump and a molecular pump (Sunshine Pumping Machinery Manufacturing Co., Ltd., Shanghai, China). During deposition, high-purity Ar (Ruida Chemical Technology Co., Ltd., Nanning, China) was introduced at a flow rate of 10 sccm, and the working pressure was maintained at 0.5 Pa. To precisely control the Ti content of the coatings, the Ni target was operated in DC mode, whereas the Ti target was operated in RF mode; the detailed sputtering parameters are listed in Table 2. Before deposition, both targets were pre-sputtered for 10 min to remove surface contaminants. To ensure coating uniformity, the sample stage was continuously rotated at 10 rpm during deposition. The coated Q420 steel specimens were subsequently gas-nitrided according to the parameters listed in Table 3 to produce duplex surface-treated (DST) specimens, with a schematic illustration of the gas-nitriding system shown in Figure 2b. The resulting nitrided specimens were designated DST-1, DST-2, DST-3, and DST-4 according to the Ti-target sputtering power. For comparison, mechanically polished Q420 steel was also subjected to gas nitriding under the conditions listed in Table 3 to produce single-nitrided Q420 steel, hereafter denoted as SN. High-purity ammonia (NH_3, Ruida Chemical Technology Co., Ltd., Nanning, China) was used as the nitriding gas.

Table 2. Magnetron sputtering parameters.

Sample	Ti Power (W)	Ni Power (W)	Time (min)
DST-1	230	70	50
DST-2	180	70	55
DST-3	130	70	60
DST-4	80	70	65

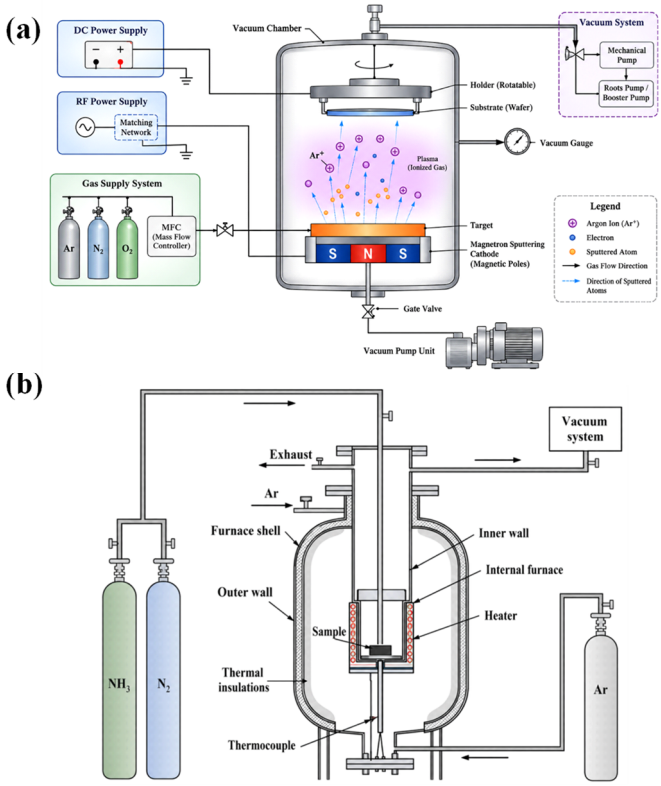


Figure 2. Schematic diagrams of the experimental setups: (**a**) magnetron sputtering system; (**b**) gas nitriding system.

Table 3. Gas nitriding parameters.

Temperature (°C)	Time (h)	Gas Flow (sccm)	Pressure
500	6	180	Atmospheric Pressure

2.2. Characterization of Properties and Microstructure

The phase composition of the samples was analyzed using an X-ray diffractometer (XRD, Rigaku Corporation, Tokyo, Japan) with Cu Kα radiation (λ = 1.5406 Å), operated at a tube voltage of 40 kV and a tube current of 40 mA, with a step size of 0.02° over a 2θ range of 10°–100°. The diffraction patterns were analyzed and indexed using Jade (MDI, 9, 2025) software. The surface and cross-sectional morphologies of the samples were examined using a scanning electron microscope equipped with an energy-dispersive X-ray spectrometer (SEM–EDS, JEOL Ltd., Tokyo, Japan), while EDS elemental mapping and line-scan analyses were performed on representative regions.

Atomic force microscopy (AFM, FEISHIMAN Ltd., Suzhou, China) was employed to characterize the surface roughness and thickness of the Ni–Ti coatings. For non-contact measurements, an OMCL-AC160TS cantilever (Olympus Corporation, Hachioji, Japan) with a spring constant of 26 N m^{-1}, a resonance frequency of 300 kHz, and an approximate tip radius of 7 nm was used. The AFM data were processed and calibrated using WSxM (2025, 5.0) software.

The Ni–Ti coatings were characterized using a field-emission transmission electron microscope (TEM, FEI Company, Hillsboro, OR, USA). Prior to TEM examination, cross-sectional TEM specimens were prepared using a focused ion beam (FIB) dual-beam system. An approximately 2 μm-thick U-shaped lamella was extracted from the coating using the ion beam, followed by alternating milling of both sides of the lamella from the front and back until electron transparency was achieved, yielding a specimen suitable for TEM observation.

The TEM images and corresponding analytical data were processed and calibrated using Gatan Digital Micrograph software.

The surface microhardness and depth-dependent hardness profiles of the samples were measured using a WHV-1MDT (Biaoyu precision instrument CO., LTD, Shanghai, China) microhardness tester in accordance with ASTM E384. Vickers hardness measurements were performed with a load of 9.807 N and a dwell time of 10 s. Hardness profiles were measured across the cross-sectional depth from 150 to 1300 μm below the sample surface. Measurements were conducted at three different locations on each specimen, and the mean value and standard deviation were calculated.

Reciprocating friction and wear tests were conducted using a UMT-3 tribometer (Bruker, Karlsruhe, Germany), as schematically illustrated in Figure 3. A silicon nitride (Si_3N_4) ball with a diameter of 6 mm and a hardness of 1500–2000 HV was employed as the counterbody. All tests were performed under dry sliding conditions at room temperature, with a sliding speed of 6 cm/s, a stroke length of 8 mm, a constant normal load of 6 N, and a test duration of 1800 s. Following the wear tests, wear-track morphologies of the nitrided specimens were subsequently examined using a laser scanning confocal microscope (Olympus Corporation, Hachioji, Japan). The cross-sectional area of each wear track was measured at four different locations, and the mean cross-sectional area and associated error were calculated. The volumetric wear loss was then estimated by multiplying the mean cross-sectional area by the wear-track length of 8 mm.

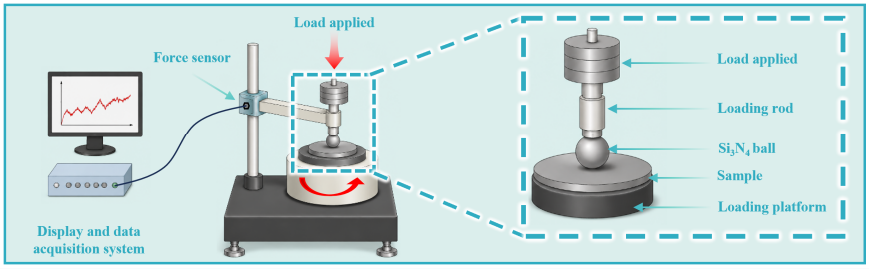


Figure 3. Schematic illustration of the tribological testing setup.

Electrochemical corrosion tests were conducted using an IM7 electrochemical workstation (Zahner Company, Kronach, Germany) in a 3.5 wt% NaCl solution. Figure 4 schematically illustrates the electrochemical testing setup. Prior to testing, the specimens were cold-mounted in resin, and an electrical wire was connected to the rear side of each specimen to establish electrical contact while leaving the exposed surface as the working area. A conventional three-electrode configuration was employed, with the specimen serving as the working electrode, a platinum mesh as the counter electrode, and a saturated calomel electrode as the reference electrode. Before electrochemical impedance spectroscopy (EIS) measurements, the specimens were immersed at open-circuit potential (OCP) for 1 h to establish a stabilized electrochemical state. EIS measurements were then performed at the stabilized OCP over a frequency range of 10^{-2}–10^{5} Hz using a sinusoidal perturbation with an amplitude of 10 mV. Potentiodynamic polarization measurements were subsequently conducted over a potential range from 500 mV below the OCP to +1.0 V, at a scan rate of 30 mV min^{-1}. To ensure data reliability and repeatability, each set of tests was repeated three times.

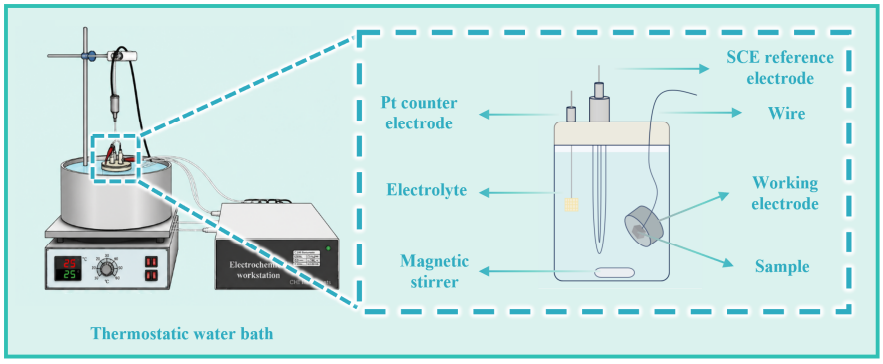


Figure 4. Schematic illustration of the electrochemical testing setup.

3. Results

3.1. Microstructure and Phase Analysis

To identify the phase constituents of the deposited coatings, XRD analysis was performed on the magnetron-sputtered samples, and the results are presented in Figure 5. In addition to the diffraction peaks originating from the Q420 steel substrate, additional reflections corresponding to metallic Ni (PDF#04–0899), Ni_3Ti (PDF#65–8314), and the B2-NiTi intermetallic phase (PDF#18–8813) were detected. This phase assemblage can be attributed to the intrinsically non-equilibrium growth conditions of dual-target magnetron sputtering and local compositional fluctuations of Ni and Ti during deposition [37]. Owing to the relatively high Ni content during deposition, Ni-rich regions preferentially retained the FCC-Ni phase, whereas local Ni-rich regions with a Ni/Ti atomic ratio approaching 3 favored the formation of Ni_3Ti [38]. Meanwhile, nanoscale regions with near-equiatomic Ni/Ti ratios may undergo short-range interdiffusion and atomic rearrangement, promoting the formation of the ordered B2-NiTi phase [39]. Such a multiphase structure is expected to generate abundant Ni/Ti-rich heterogeneous interfaces, which may facilitate the adsorption and dissociation of NH_3.

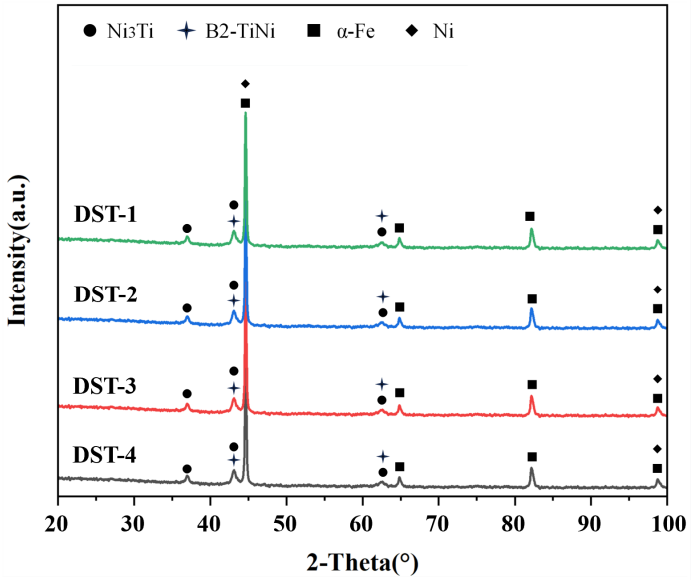


Figure 5. XRD pattern of specimen surfaces after magnetron sputtering.

To further elucidate the microstructure of the coating, TEM analysis was performed on the magnetron-sputtered DST-4 sample. Figure 6a shows the FIB-prepared cross-sectional specimen of the Ni–Ti coating, and EDS analysis indicates that the examined region is rich in

Ni and Ti, with a minor amount of O. Further analysis of the high-resolution TEM image in Figure 6b, together with the fast Fourier transform (FFT) and inverse fast Fourier transform (IFFT) analyses of a representative region shown in Figure 6c, yielded an interplanar spacing of 2.18 Å. This spacing is consistent with the (110) plane of the B2-NiTi phase, as determined from the selected-area electron diffraction (SAED) pattern in Figure 6e. The interplanar spacings calculated from the diffraction pattern in Figure 6e are approximately 2.16, 1.52, 1.25, 0.97, and 0.89 Å, corresponding to the (110), (200), (211), (310), and (222) planes of B2-NiTi, respectively. The close agreement between these interplanar spacings and the characteristic lattice spacings of B2-NiTi, together with the XRD results, provides further evidence for the presence of the B2-NiTi phase within the coating.

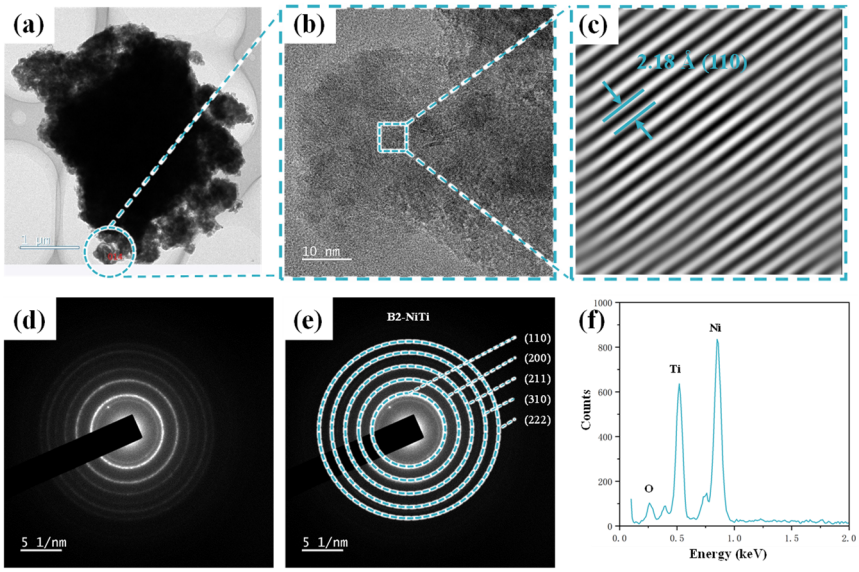


Figure 6. (**a**) FIB-prepared cross-sectional image of the DST-4 sample; (**b**) high-resolution TEM image of the selected region; (**c**) IFFT pattern of the selected region in (**b**); (**d**,**e**) SAED patterns acquired from the region shown in (**a**); (**f**) EDS spectrum of the selected region.

Figure 7 presents the surface morphology, elemental distribution, and cross-sectional structure of the Ni–Ti coatings deposited under different magnetron sputtering conditions. As shown in Figure 7a–d, all specimens exhibited continuous and relatively uniform surface coverage, with no large-area pores, through-thickness cracks, or pronounced delamination observed, indicating that dual-target magnetron sputtering can produce well-covered Ni–Ti coatings on Q420 steel. EDS analysis further confirmed the systematic regulation of the chemical composition of the films. Based on the corresponding elemental atomic masses, the atomic fraction of Ni, expressed as Ni/(Ni + Ti), is summarized in Table 4. An Fe signal of approximately 9.4–11.3 wt.% was detected by EDS; given the relatively small film thickness of approximately 1μm, this signal is most likely attributable to the contribution of the Q420 steel substrate within the electron interaction volume and therefore should not be directly interpreted as the actual Fe content of the film [40]. Cross-sectional SEM observations further revealed the film thickness and interfacial structural characteristics. As shown in Figure 7(a1–d1), all specimens developed continuous surface layers with relatively well-defined interfaces with the Q420 steel substrate. The corresponding film thicknesses of DST-1, DST-2, DST-3, and DST-4 were 1.34, 1.38, 1.36 and 1.34 μm, respectively.

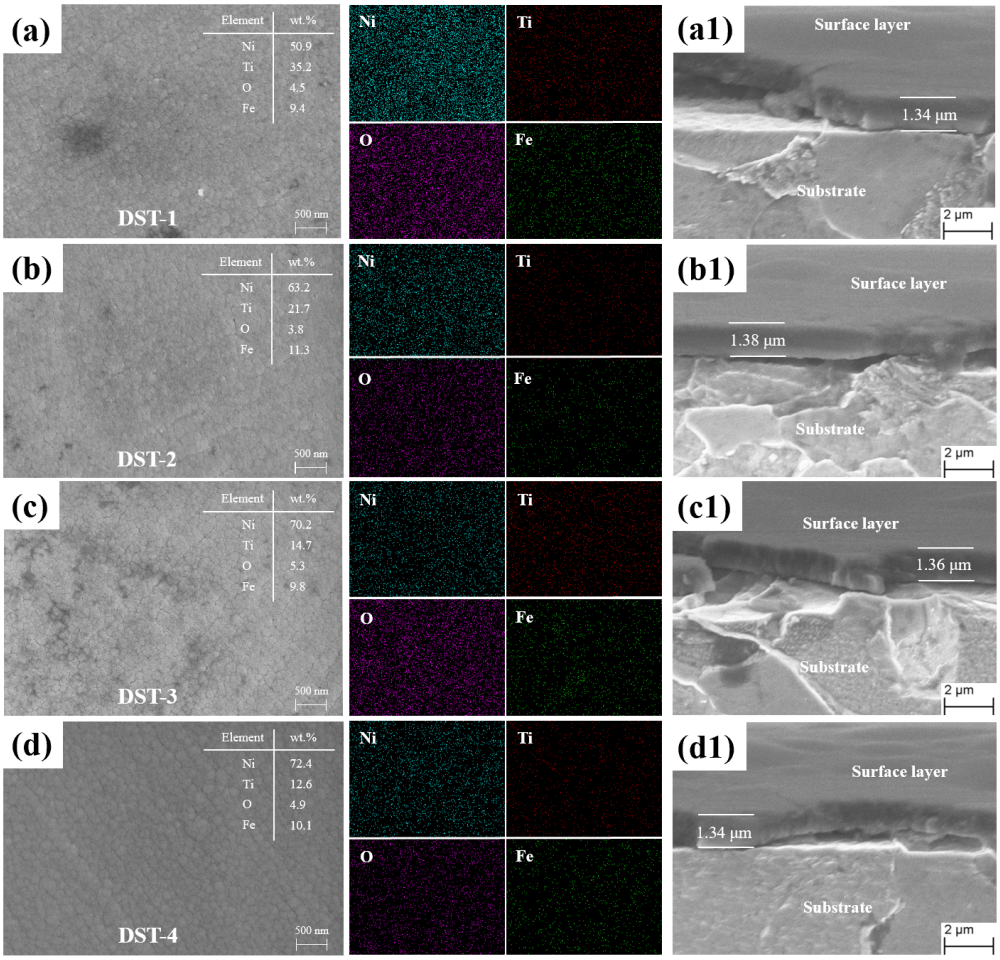


Figure 7. (**a**–**d**) Surface SEM images and EDS mapping of the specimens after magnetron sputtering; (**a1**–**d1**) cross-sectional SEM images of the specimens after magnetron sputtering.

Table 4. Atomic percentage of Ni/(Ni + Ti) in the coatings.

Samples	Ni wt.%	Ni/(Ni+Ti) at.%
DST-1	50.9	54.1
DST-2	63.2	70.4
DST-3	70.2	79.6
DST-4	72.4	82.4

To further characterize the surface morphology of the Ni–Ti films, AFM analysis was performed on the Ni–Ti coatings, as shown in Figure 8. Figure 8a shows that the Ni–Ti coating has an overall continuous surface with micro- to nanoscale undulations composed of numerous fine peaks and valleys. The three-dimensional topography further reveals a relatively continuous distribution of surface peaks, valleys, and ridge-like features throughout the scanned area, with no large-area pores or pronounced through-thickness defects observed, indicating good surface continuity of the Ni–Ti film. To further elucidate the local microstructure, a selected region in Figure 8a was examined at higher magnification. Compared with the larger-scale scanned area, the magnified region exhibits more pronounced peak-to-valley undulations. The height distribution in Figure 8(b3) remains characterized by a relatively concentrated unimodal profile, indicating that although pronounced peak-to-valley features are present in this local region, the overall height distribution remains relatively uniform. These surface undulations are more likely associated with local mor-

phological variations arising from nucleation, island growth, and grain coalescence during film deposition, rather than large-scale film instability or severe delamination.

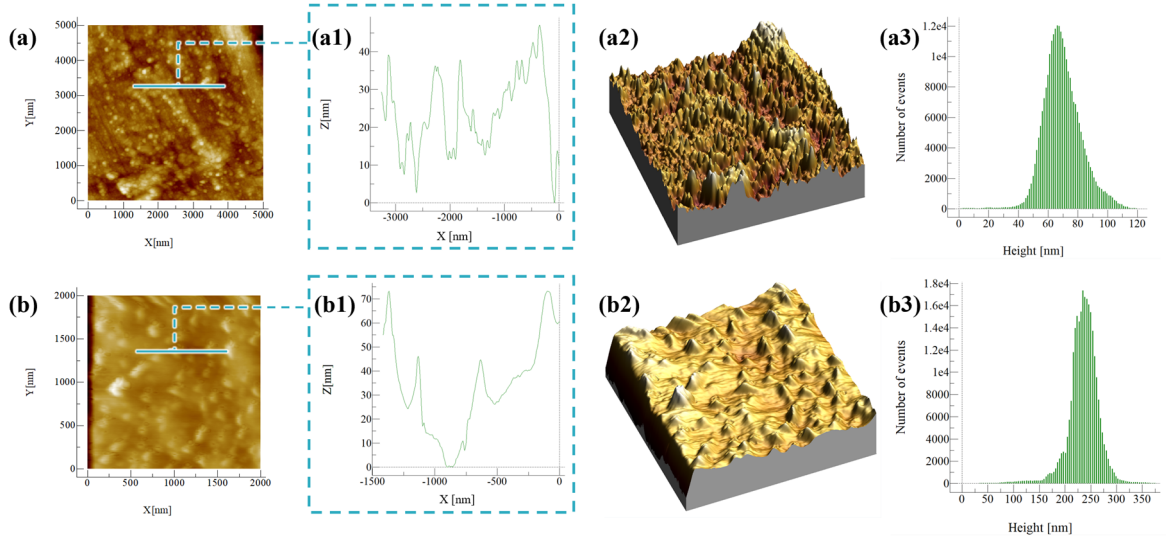


Figure 8. (**a**–**a3**) corresponding AFM characterization of the Ni-Ti coating surface; (**b**–**b3**) enlarged AFM characterization of the selected region in (**b**).

In order to evaluate the promoting effect of the Ni–Ti coating on the gas nitriding behavior of Q420 steel, cross-sectional SEM characterization was performed on specimens with different Ni–Ti compositions and on the untreated sample, as shown in Figure 9a–e. Quantitative analysis revealed that the nitrided layer thicknesses of DST-2, DST-3, and DST-4 were all greater than that of SN, with DST-2 exhibiting the thickest nitrided layer of 8.78 μm, approximately 2.3 times that of SN. Consistent with the aforementioned EDS results, the nitrided-layer thickness exhibited a pronounced non-monotonic dependence on Ni content, reaching a maximum at approximately 70 at.% Ni. The EDS nitrogen depth profiles a1–e1 further corroborate these observations, exhibiting intense N signals near the surface followed by attenuation at varying depths, with the inflection points of these signal transitions providing a clear indication of the effective interfaces between the nitrided layers and the underlying substrates. Furthermore, DST-2 exhibited a relatively high nitrogen signal intensity at greater depths compared with SN, indicating that the introduction of the catalytic coating effectively promoted the inward diffusion of reactive nitrogen species. Compared with SN, DST-2 exhibited a clearly distinguishable interface between the nitrided layer and the substrate, together with a denser microstructure within the nitrided layer, further confirming the advantages of catalytic nitriding in promoting deep nitrogen diffusion and improving the structural integrity of the nitrided layer. This finding suggests that the promoting effect of the Ni–Ti system on gas nitriding is not governed simply by the Ni content, but may instead arise from a composition-dependent synergistic interaction between Ni and Ti. At an appropriate Ni/Ti ratio, Ni active sites and the interfacial electronic structure of the Ni–Ti system may jointly regulate NH_3 adsorption and dissociation, thereby enhancing the supply of reactive nitrogen species at the surface and facilitating their inward transport into the steel substrate [41].

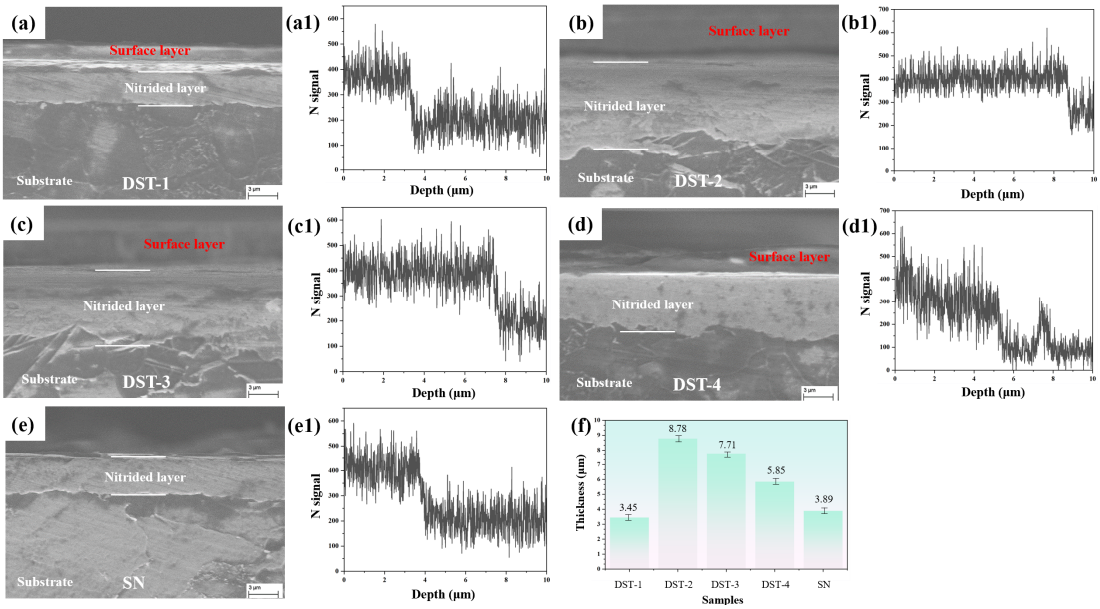


Figure 9. (**a**–**e**) Cross-sectional SEM images of the specimens after nitriding; (**a1**–**e1**) N signal intensity by EDS as a function of the distance from the sample surface; (**f**) statistical analysis of the thickness of the nitrided layer.

Figure 10a–e presents the surface morphology of the samples after nitriding. The results indicate that the Ti content significantly influences the precipitation behavior and morphology of nitrides on the Ni–Ti coating surface. As the Ti content decreased from DST-1 to DST-4, the surface morphology evolved from densely packed, fine particles to coarsened and agglomerated nodular features in DST-3, whereas severe network-like cracking developed in DST-4, which had the lowest Ti content, owing to volume expansion and stress concentration associated with localized nitride precipitation. This behavior may be attributed to excessive surface nitride precipitation caused by the high Ti content in DST-1, resulting in an overly thick, dense surface layer that severely impedes further inward diffusion of nitrogen atoms and consequently deteriorates the catalytic performance. In contrast, DST-2 achieved an optimal balance between Ti content and nitride-layer thickness; the moderately developed nitride layer not only avoided impeding nitriding but also favorably modified the surface activity and structure. The SN sample exhibited a dense and uniform polyhedral compound layer on its surface, without obvious macroscopic cracks.

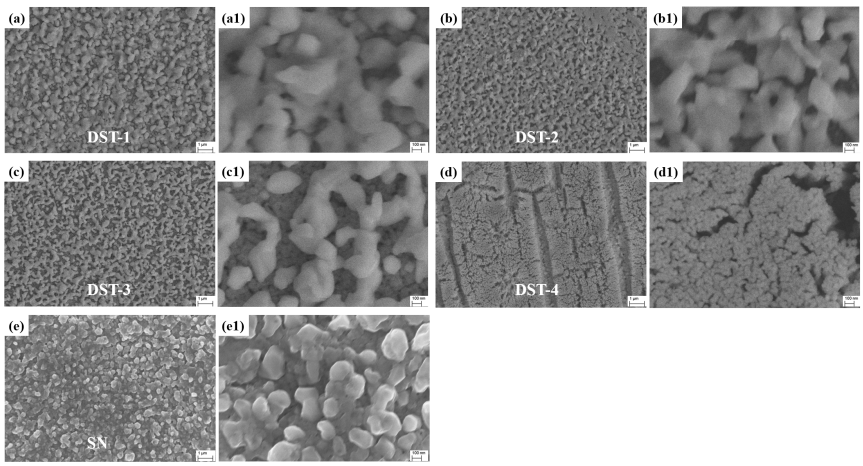


Figure 10. (**a**–**e**) Surface morphologies of the samples after nitriding; (**a1**–**e1**) corresponding higher-magnification images.

The XRD patterns of the SN, SNN, and SNT specimens after gas nitriding are presented in Figure 11, revealing distinct differences in their surface phase composition. The diffraction peaks of the SN specimens are primarily associated with iron nitrides of different stoichiometries. This suggests that without a catalytic coating, nitrogen atoms primarily combine with Fe in the substrate via conventional thermally activated diffusion. After introducing the Ni-Ti coating, the diffraction pattern changes significantly. In addition to the FeN phase, distinct diffraction peaks corresponding to metallic Ni and Fe_3N are also observed. This suggests that the Ni coating acts as a catalytic medium during nitriding, potentially promoting NH_3 adsorption and dissociation while also participating in interfacial chemical reactions that lead to the formation of nickel nitrides. Notably, all the coated specimens exhibit a complex multiphase composition with diffraction peaks attributed to Ni, FeN, Ni_3N, and Fe_3N alloy phases. The identification of TiN and $FeNi_3$ suggests that the Ni-Ti coating undergoes compositional and structural changes during nitriding rather than remaining an unchanged surface layer [42,43]. Overall, the XRD results indicate that Ni-Ti coating modification influences the formation and distribution of nitrided phases, potentially contributing to the improved nitriding behavior of the Q420 steel substrate.

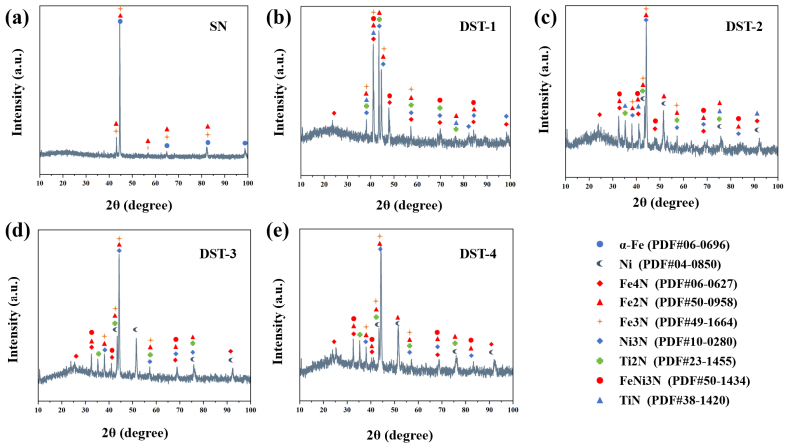


Figure 11. XRD patterns of different specimens after nitriding: (**a**) SN specimen; (**b**) DST-1 specimen; (**c**) DST-2 specimen; (**d**) DST-3 specimen; (**e**) DST-4 specimen.

3.2. Microhardness

Figure 12 presents the in-depth microhardness profiles and surface microhardness of the specimens. The untreated sample exhibited a relatively stable microhardness of approximately 200 HV. In contrast, all nitrided samples exhibited pronounced hardness gradients, indicating the progressive inward diffusion of nitrogen from the surface and the formation of nitrided layers with continuous hardness gradients. Notably, DST-1 exhibited a surface microhardness of 843.24 HV, representing increases of approximately 24.9% relative to SN (675.24 HV) and 319.9% relative to the untreated sample (200.84 HV). As shown in Figure 9, the nitrided layer thickness of the DST-1 sample is approximately 3.45 μm, which is considerably smaller than that of DST-2 (8.78 μm), whereas the measured surface microhardness is highest for DST-1. Although this observation may appear contradictory at first glance, the overall nitrided layer thickness and surface microhardness do not necessarily exhibit a monotonic correlation. The nitrided layer thickness primarily reflects the depth of the hardened zone and its load-bearing capacity, whereas surface microhardness characterizes the resistance of localized surface regions to plastic deformation, with both properties being jointly influenced by factors such as the composition and density of the surface compound layer, phase structure, grain size, residual stress, and defect distribution [44,45]. Although the DST-1 sample exhibits a relatively thin nitrided layer, the formation of a more continuous

and compact compound layer at its surface accounts for its higher surface microhardness. With increasing depth, the hardness of all nitrided samples gradually decreased and approached that of the untreated substrate at depths of approximately 900 μm. This behavior can be attributed to the inward diffusion of nitrogen during nitriding, which promotes the formation of numerous fine alloy nitrides and consequently induces pronounced precipitation and solid-solution strengthening, leading to a substantial increase in hardness. Beyond the effective diffusion zone of reactive nitrogen species, the nitrogen concentration falls below the solid-solubility limit, and the microstructure gradually approaches the original quenched-and-tempered state, causing the hardness to converge toward that of the untreated substrate [40]. Notably, the effective hardened-layer depth determined in Figure 12 was substantially greater than the nitrided-layer thickness observed in the SEM images in Figure 9. This discrepancy arises from the different response mechanisms of the characterization techniques to microstructural changes. SEM images and EDS signals primarily characterize regions where pronounced microstructural changes occur, such as extensive nitride precipitation, whereas the deeper hardened region corresponds to a solid-solution-strengthened zone in which the concentration of nitrogen diffusing into the substrate is relatively low. Although no distinct nitride precipitates form in this region, interstitial nitrogen atoms in solid solution can still induce substantial lattice distortion, thereby impeding dislocation motion and maintaining elevated hardness.

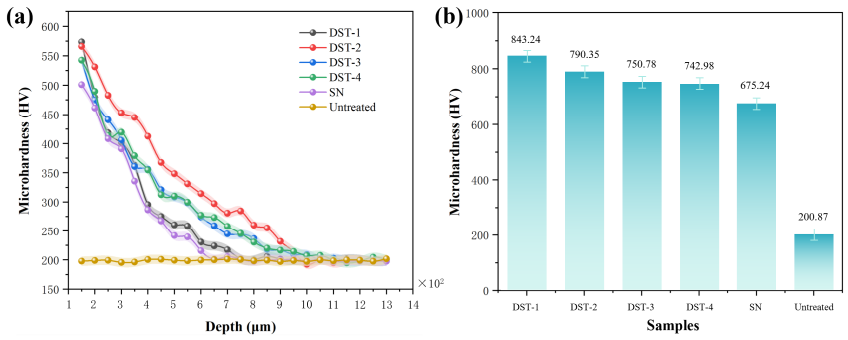


Figure 12. (**a**) In-depth microhardness profiles of the specimens; (**b**) surface microhardness of the specimens.

3.3. Tribology

As shown in Figure 13, the average coefficients of friction (COF) of the samples were 0.386 for DST-1, 0.393 for DST-2, 0.397 for DST-3, 0.406 for DST-4, 0.419 for SN, and 0.453 for the untreated sample. As a fundamental physical parameter characterizing frictional resistance at the tribological interface, the COF substantially influences material wear behavior through energy dissipation, thermal effects, and interfacial stability. A higher COF indicates that more energy is required to overcome frictional resistance under the same applied load, with most of this energy being dissipated as frictional heat, thereby increasing the interfacial temperature [46]. Elevated temperatures can not only soften the material substrate and accelerate oxidation but also promote the deterioration of wear mechanisms, thereby accelerating material loss. Furthermore, fluctuations in the coefficient of friction (COF) are also significant, as the relatively stable COF curves in Figure 13a, particularly those of DST-2 to DST-4, indicate the formation of dynamically stable tribological interfaces associated with gradual and mild wear. In contrast, the pronounced fluctuations observed for DST-1 between 25 and 30 min may indicate disruption of the surface tribofilm, abnormal debris accumulation, or localized material delamination, suggesting potential deterioration of the wear process accompanied by an increased wear rate. Overall, DST modification effectively reduced the COF from 0.453 for the untreated sample to a range of 0.386–0.406.

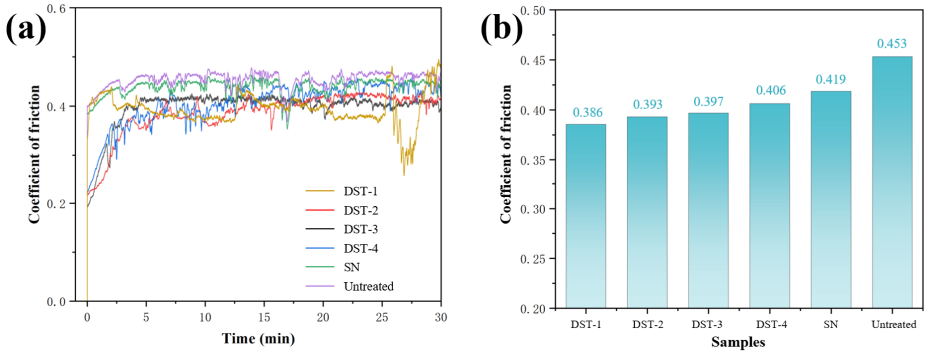


Figure 13. (**a**) COF curves of the specimens; (**b**) average COF of the specimens.

By integrating the quantitative data in Table 5 with the morphological and elemental characterizations presented in Figure 14, this study systematically elucidates the evolution of tribological properties and wear mechanisms under different treatment conditions. The untreated sample exhibited the poorest wear resistance, with the widest and deepest wear track (223.7 μm and 6.74 μm, respectively) and a wear volume as high as 9.227×10^6 μm^3. Its SEM morphology revealed pronounced deep and wide grooves accompanied by fatigue-induced spallation pits, together with a strong oxygen (O) signal, indicating severe combined damage involving abrasive wear, adhesive spallation, and oxidative wear of the substrate. Following DST treatment, the wear volume decreased substantially, with DST-2 exhibiting the best overall performance, reducing the wear volume to 1.623×10^6 μm^3, corresponding to an 82.4% reduction. SEM observations revealed relatively narrow, shallow, and smooth wear tracks for the DST-treated samples, with DST-2 exhibiting the most compact morphology, indicating effective suppression of plastic deformation and material loss. EDS elemental mapping further elucidated the tribochemical behavior at the sliding interface. In addition to the surface-strengthening element N, pronounced Si and O enrichment was observed within the wear tracks of the DST-treated samples. These findings suggest that, under friction-induced stresses, material transfer from the Si-containing counterface occurred, followed by in situ tribochemical reactions with ambient oxygen, resulting in the formation of a compact Si/O-rich tribo-oxidative film [47]. In summary, the untreated sample was predominantly subjected to severe abrasive and oxidative wear, whereas DST treatment not only achieved surface strengthening through N incorporation but also promoted the formation of an in situ triboprotective film, shifting the dominant wear mechanisms toward mild abrasive wear and tribochemical film-mediated protection [48]. Among the DST-treated samples, DST-2 achieved the optimal balance between surface strengthening and triboprotective film formation, thereby exhibiting outstanding wear resistance.

Table 5. Dimensions of the wear tracks of different specimens.

Samples	Wear-Track Width (μm)	Wear-Track Depth (μm)	Wear Volume ($\times 10^6$ μm^3)
Untreated	223.7	6.7	9.227 ± 0.21
SN	201.4	4.2	5.184 ± 0.17
DST-1	95.7	5.4	3.086 ± 0.23
DST-2	84.3	3.3	1.623 ± 0.20
DST-3	71.4	5.0	2.186 ± 0.21
DST-4	98.6	4.2	2.474 ± 0.22

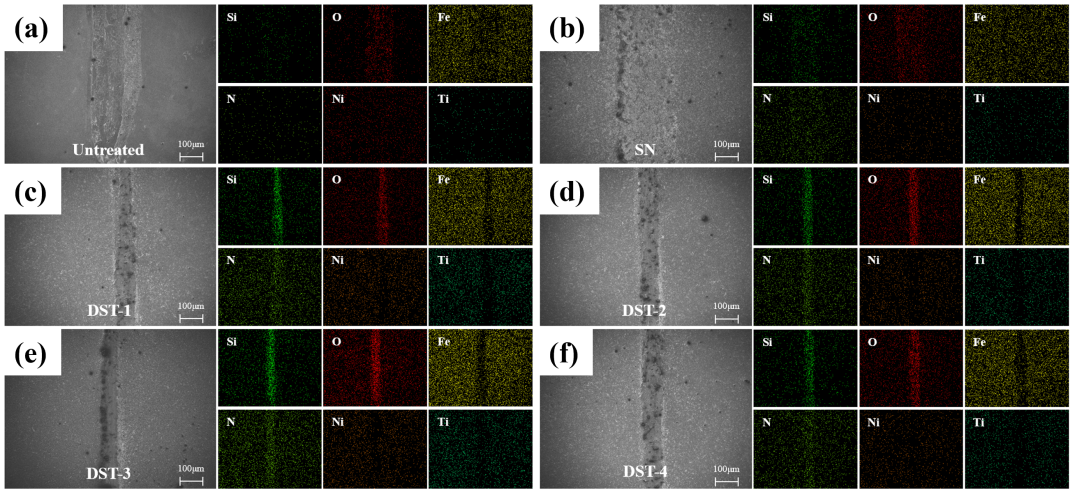


Figure 14. SEM images and elemental mapping of the wear tracks. (**a**) Untreated; (**b**) SN; (**c**) DST-1; (**d**) DST-2; (**e**) DST-3; (**f**) DST-4.

3.4. Electrochemical Corrosion

Figure 15a presents the potentiodynamic polarization curves of the specimens. The corrosion potential Ecorr and corrosion current density Icorr were determined using the Tafel extrapolation method, and the corresponding values are summarized in Table 6. The untreated sample exhibited an Ecorr of −376.59 mV and an Icorr of 0.390 mA cm^{-2}, indicating relatively high corrosion activity. After gas nitriding, Ecorr shifted positively by 81.2 mV to −295.39 mV, while Icorr decreased by 32.3% to 0.264 mA cm^{-2} relative to the untreated sample. Following DST treatment, the electrochemical stability of the specimens was further improved. In particular, DST-2 exhibited an Icorr of 0.191 mA cm^{-2}, corresponding to reductions of 51.0% and 27.7% relative to the untreated and SN samples, respectively. Meanwhile, its Ecorr of −143.26 mV represented a positive shift of 233.33 mV relative to the untreated sample. Figure 15b–d shows the EIS spectra of the specimens after 1 h of open-circuit potential stabilization in 3.5% NaCl solution. The Nyquist plots show that the capacitive arcs of the DST-treated specimens have larger radii than those of the SN and untreated samples, indicating higher interfacial impedance and thus greater resistance to electrochemical reactions. It was mainly caused by the charging and discharging process of the surface rust layers. The low-frequency region showed an obvious inductive arc, indicating that the corrosion product absorbed and desorbed during the corrosion process. The inductive loop at low frequencies may be associated with the relaxation of adsorbed intermediate species and/or the dynamic evolution of corrosion products during localized dissolution and repassivation. The appearance of an inductive loop was a dispersion effect of the corrosion products [49]. In the modal diagram of the Bode diagram, the impedance value in the low-frequency region represented the charge transfer resistance. It then reflected the degree of difficulty in the electrode reaction. The larger the impedance value, the larger the reaction resistance [50,51]. Overall, DST-2 exhibited the best corrosion resistance, whereas the difference in corrosion resistance between the untreated and SN samples was relatively small.

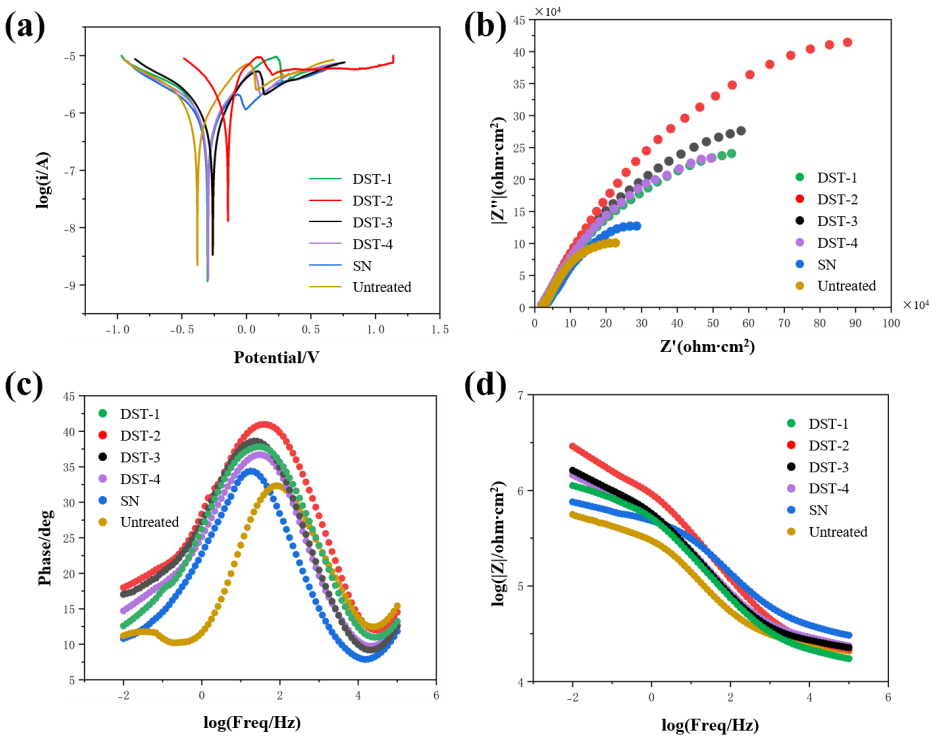


Figure 15. The test results of the specimens in a 3.5% NaCl solution: (**a**) potentiodynamic polarization curves; (**b**) Nyquist plots; (**c**,**d**) Bode plots.

Table 6. Corrosion properties of the untreated and treated samples.

Sample	E_{corr} (mV)	I_{corr} (mA/cm^2)
Untreated	−376.59	0.390
SN	−295.39	0.264
DST-1	−296.79	0.248
DST-2	−143.26	0.191
DST-3	−170.17	0.240
DST-4	−288.30	0.246

Figure 16 presents the surface SEM images of the specimens after electrochemical testing. After electrochemical testing, the untreated sample exhibited pronounced localized corrosion, with relatively large dark corrosion pits observed on the surface, indicating that Cl^- ions could readily penetrate the surface and induce localized anodic dissolution. DST treatment further modified the surface corrosion morphology of the nitrided layer after polarization. As shown in Figure 16d, the DST-2 specimen retained the most intact and homogeneous surface morphology, with no pronounced localized corrosion regions, indicating the strongest resistance to anodic dissolution and the highest surface electrochemical stability among the specimens. This observation is consistent with the enhanced corrosion resistance revealed by the EIS and potentiodynamic polarization measurements, demonstrating that DST treatment improves the microstructural integrity of the nitrided layer and effectively suppresses the corrosion of Q420 steel.

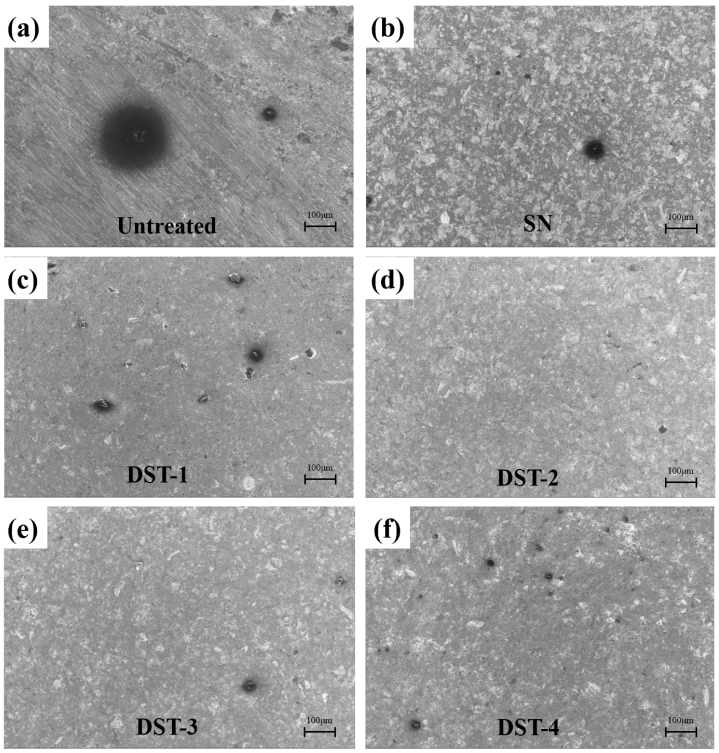


Figure 16. SEM images of the corroded specimen surfaces. (**a**) Untreated; (**b**) SN; (**c**) DST-1; (**d**) DST-2; (**e**) DST-3; (**f**) DST-4.

4. Conclusions

This study investigated the effects of Ni–Ti coating-assisted gas nitriding on the surface characteristics, mechanical properties, and corrosion resistance of Q420 steel. Based on the microstructural and property characterization, the following conclusions can be drawn:

1. Composition-controlled Ni–Ti coatings were successfully deposited on Q420 steel via dual-target magnetron sputtering. The coatings exhibited continuous surface coverage and a multiphase structure involving Ni-, Ni_3Ti- and B2-NiTi-related phases.
2. The Ni–Ti interlayer substantially enhanced the gas-nitriding response of Q420 steel under otherwise identical nitriding conditions. The nitrided-layer thickness exhibited a pronounced dependence on Ni content rather than a monotonic trend. A maximum nitrided-layer thickness of 8.78 μm was achieved for DST-2 containing 70.4 at.% Ni, approximately 2.3 times that of the corresponding SN sample.
3. Ni–Ti-assisted nitriding substantially enhanced the surface mechanical properties of Q420 steel. Nitriding produced a pronounced hardness gradient, with the surface hardness of DST-1 reaching 843.24 HV compared with approximately 200 HV for untreated Q420 steel. The enhanced hardness is attributed to nitrogen-induced solid-solution strengthening and precipitation strengthening associated with nitride formation in the near-surface region.
4. The DST-2 sample exhibited an exceptionally low wear volume of only 1.623×10^6 μm^3, representing reductions of approximately 82.4% and 68.7% compared with the untreated and conventionally nitrided samples, respectively. The improved wear resistance was primarily attributed to the increased thickness and enhanced load-bearing capacity of the hardened nitrided layer.
5. Ni–Ti-assisted nitriding also enhanced the electrochemical stability of Q420 steel. DST-2 exhibited the most positive corrosion potential (−143.26 mV) and the lowest corrosion current density (0.191 mA cm^{-2}). Collectively, these results demonstrate that

optimized Ni–Ti-assisted nitriding can simultaneously enhance the mechanical and electrochemical performance of Q420 steel.

Author Contributions: Writing—original draft, formal analysis, H.S.; software, J.L. and H.S.; data curation, M.C. and X.L.; investigation, J.L.; resources, M.C. and X.L.; methodology, J.L.; validation, J.L. and H.S.; visualization, M.C. and J.L.; writing—review and editing, supervision, H.S. and J.L. All authors have read and agreed to the published version of the manuscript.

Funding: This research was funded by National Natural Science Foundation of China, grant number 22362005; Ph.D. Programs Foundation of Guangxi University of Science and Technology, grant number 23Z04; Guangxi Science and Technology Program, grant number Gui Ke LT2600640037. And The APC was funded by Junming Li.

Institutional Review Board Statement: Not applicable.

Informed Consent Statement: Not applicable.

Data Availability Statement: The original contributions presented in this study are included in the article. Further inquiries can be directed to the corresponding author.

Conflicts of Interest: The authors declare no conflict of interest.

References

1. Ding, F.X.; Lan, L.F.; Yu, Y.J.; Man, M.K. Experimental study of the effect of a slow-cooling heat treatment on the mechanical properties of high strength steels. *Constr. Build. Mater.* **2020**, *241*, 118020. [CrossRef]
2. Sun, Y.; Song, D.; Sun, S.; Guo, Y.; Zhao, Q. Buckling behavior and design of large-size and high-strength steel angle under combined compression and biaxial bending. *Thin-Walled Struct.* **2025**, *212*, 113124. [CrossRef]
3. Zhang, Z.; Han, J.-Y.; Luo, L.; Zhu, B.; Liu, Y.-L.; Cui, S.-A.; Wang, X.-W. Experimental study on the mechanical behavior of steel in anchor systems of steel anchor boxes for long-span cable-stayed bridges. *Constr. Build. Mater.* **2025**, *485*, 141918. [CrossRef]
4. Yang, J.-J.; Zhao, K.-W.; Fan, M.; Gao, Q.; Zhou, W.-H.; Fan, C.-H.; Lu, Q.-J.; Miao, W.-S.; Luo, D.; Chen, Q.; et al. Effect of different stabilizers on corrosion resistance and damage resistance of Q420qNH weathering steel in industrial atmospheric environment. *Constr. Build. Mater.* **2025**, *490*, 142398. [CrossRef]
5. Wang, J.; Di, J.; Zheng, Y.; Qin, F.; Su, Y. Interactive buckling behaviour of Q420–Q960 steel welded thin-walled H-section long column. *Thin-Walled Struct.* **2024**, *203*, 112219. [CrossRef]
6. Holmberg, K.; Erdemir, A. The impact of tribology on energy use and CO_2 emission globally and in combustion engine and electric cars. *Tribol. Int.* **2019**, *135*, 389–396. [CrossRef]
7. Holmberg, K.; Erdemir, A. Influence of tribology on global energy consumption, costs and emissions. *Friction* **2017**, *5*, 263–284. [CrossRef]
8. Li, Z.; Ma, L.; Ren, C.; Wang, J.; Tian, R.; Chen, Z.; Chen, W.; Li, X.; Zhang, D. Accelerated rust stabilization for weathering steels via a high-throughput approach. *Corros. Sci.* **2025**, *244*, 112645. [CrossRef]
9. Chu, H.; Zhai, J.; Guan, Y.; Chen, F.; Lin, J. Stages and mechanism of Q420B hot-dip galvanized steel corrosion in simulated dry/wet coastal atmosphere. *Corros. Sci.* **2025**, *245*, 112710. [CrossRef]
10. Kücükyildiz, Ö.C.; Grumsen, F.B.; Christiansen, T.L.; Winther, G.; Somers, M.A.J. Anisotropy effects on gaseous nitriding of austenitic stainless steel single crystals. *Acta Mater.* **2020**, *194*, 168–177. [CrossRef]
11. Guo, T.; Chen, Y.; He, C.; Liang, Z.; Zhao, Q. Effects of boriding and nitriding on the corrosion and erosion behavior of martensitic heat-resistant steels in the supercritical CO_2 at 600 °C. *Corros. Sci.* **2025**, *252*, 112966. [CrossRef]
12. Liu, B.; Wang, B.; Yang, X.; Zhao, X.; Qin, M.; Gu, J. Thermal fatigue evaluation of AISI H13 steels surface modified by gas nitriding with pre- and post-shot peening. *Appl. Surf. Sci.* **2019**, *483*, 45–51. [CrossRef]
13. Chen, Y.; Liu, C.; Yan, H.; Fan, Y.; Wang, J.; Cui, Y. Effect of gas nitriding on 316 L stainless steel lattice manufactured via selective laser melting. *Surf. Coat. Technol.* **2022**, *441*, 128559. [CrossRef]
14. Hinrichs, R.; Vasconcellos, M.A.Z.; Amaral, L.; Oliveira, L.F.; Rocha, A.D.S. Simple procedure to establish thickness and phase composition of plasma nitrided and post-oxidized steel surfaces using multiple angle GIXRD and RIR quantification. *Appl. Surf. Sci.* **2025**, *685*, 162079. [CrossRef]
15. Kang, K.; Kwon, S.; Lee, C.; Hong, D.; Lee, H.M. Hierarchical analysis of alloying element effects on gas nitriding rate of Fe alloys: A DFT, microkinetic and kMC study. *Acta Mater.* **2019**, *174*, 173–180. [CrossRef]
16. Niu, J.B.; Waqas Qureshi, M.; Ding, Z.F.; Ma, X.X.; He, Y. Effect of nitriding on the transformation of alloy carbides (VC and Mo2C) in 8Cr4Mo4V steel. *Appl. Surf. Sci.* **2023**, *610*, 155561. [CrossRef]

17. Yang, Y.; Dai, X.Z.; Yang, X.R.; Zhang, S.H.; Li, D.Y. First-principles analysis on the role of rare-earth doping in affecting nitrogen adsorption and diffusion at Fe surface towards clarified catalytic diffusion mechanism in nitriding. *Acta Mater.* **2020**, *196*, 347–354. [CrossRef]
18. Liang, K.; Wang, J.; Wang, G.; Zhang, J.; Zou, W.; Wei, Z.; Pan, Y.; He, G.; Du, R.; Chen, L.; et al. Effect of micro-shot peening on the rolling contact fatigue performance of nitrided steel at elevated temperature. *Eng. Fail. Anal.* **2026**, *196*, 111128. [CrossRef]
19. Jafarpour, S.M.; Leineweber, A.; Bolan, M.; Dalke, A.; Biermann, H. Effectiveness of surface activation induced by different methods during afterglow plasma nitrocarburizing of AISI 316L. *Surf. Coat. Technol.* **2025**, *502*, 131980. [CrossRef]
20. Yang, S.; Liang, Y.; Chen, P.; Zhang, H.; Shang, X.; Wang, P. Construction of a multilayer coating on MP159 superalloy via the sputtering-nitriding duplex treatment and its tribological behavior. *Mater. Charact.* **2026**, *236*, 116439. [CrossRef]
21. Li, J.; Shao, H.; Lu, K. A review of the corrosion and wear resistance mechanisms of gas nitriding on steel. *iScience* **2026**, *29*, 115048. [CrossRef] [PubMed]
22. Ma, Q.; Jia, S.; Liu, Q.; Shang, C. Effects of Cr and Ni addition on critical crack tip opening displacement (CTOD) and supercritical CO_2 corrosion resistance of high-strength low-alloy steel (HSLAs). *Mater. Sci. Eng. A* **2024**, *908*, 146772. [CrossRef]
23. Wang, L.; Wei, Y.; Ma, J.; Zhang, S.; Liu, B.; Wu, H.; Wu, P.; Feng, Y.; Zhang, Y. Optimizing the resistance of Cr-advanced steel to CO_2 corrosion with the addition of Ni. *J. Mater. Res. Technol.* **2024**, *32*, 97–111. [CrossRef]
24. Xu, Z.; Hou, Y.; Nele, M.; Li, G.; Zhou, S. High-throughput first-principles study on the effect of Ni segregation on the formation of Cr-depleted zone and corrosion resistance of S32205 duplex stainless steels. *J. Mater. Res. Technol.* **2024**, *30*, 3474–3484. [CrossRef]
25. Akhter, R.; Zhou, Z.; Xie, Z.; Munroe, P. Harmonizing mechanical responses of nanostructured CrN coatings via Ni additions. *Appl. Surf. Sci.* **2021**, *538*, 147987. [CrossRef]
26. Pichon, L.; Dubois, J.-B.; Chollet, S.; Larek, F.; Cormier, J.; Templier, C. Low temperature nitriding behaviour of Ni_3Al-like γ' precipitates in nickel-based superalloys. *J. Alloys Compd.* **2019**, *771*, 176–186. [CrossRef]
27. Tima, R.; Mahboubi, F. Ability of plasma nitriding to improve tribological behavior of medium and high boron electroless nickel coatings. *Tribol. Int.* **2021**, *156*, 106822. [CrossRef]
28. Mirhosseini, S.S.; Mahboubi, F. Effect of plasma nitriding on tribological properties of nickel-boron-nanodiamond electroless coatings. *Surf. Coat. Technol.* **2022**, *435*, 128216. [CrossRef]
29. Chen, F.; Jiang, H.; Tian, S.; Zhang, Y.; Zhang, R.; Wu, Y.; Yang, Y.; Liu, W.; Zhang, S.; Hong, Z.; et al. First-principles calculations on the mechanism of catalytic nitriding by Cr or Ni microalloying. *Appl. Surf. Sci.* **2025**, *711*, 164017. [CrossRef]
30. Moskovkin, P.; Maszl, C.; Schierholz, R.; Breilmann, W.; Petersen, J.; Pflug, A.; Muller, J.; Raza, M.; Konstantinidis, S.; von Keudell, A.; et al. Link between plasma properties with morphological, structural and mechanical properties of thin Ti films deposited by high power impulse magnetron sputtering. *Surf. Coat. Technol.* **2021**, *418*, 127235. [CrossRef]
31. Tiwari, S.K.; Rao, A.U.; Kharb, A.S.; Chawla, V.; Pandey, J.K.; Saxena, V.; Sardana, N.; Avasthi, D.K.; Chawla, A.K. Microstructural and Mechanical Properties of Cr-Ni3Al Alloy Films Synthesized by Magnetron Sputtering. *J. Mater. Eng. Perform.* **2024**, *33*, 8994–9003. [CrossRef]
32. Margono; Darmadi, D.B.; Gapsari, F.; Widodo, T.D.; Kartika, B.M. Enhanced corrosion resistance of aluminum 6061 alloy using Ti-based thin films and plasma nitriding. *JCIS Open* **2025**, *18*, 100139. [CrossRef]
33. Wang, Y.; Zhang, G.; Wu, Y.; Zheng, Y.; Wang, H.; Li, Y.; Cao, X.; Meng, X.; Gao, Z.; Yi, X. Achieving ultrahigh microhardness and superior wear resistances in 60NiTi alloys towards bearing applications. *Chin. J. Aeronaut.* **2025**, *38*, 103776. [CrossRef]
34. Gong, W.; Yang, B.; Chen, H.; Chen, Y.; Shen, X.; Hao, W.; Wang, X.; Huang, L. Effects of Ce-La rare earth microalloying on the microstructure and corrosion characteristics of Q420 high-strength steel. *Int. J. Electrochem. Sci.* **2023**, *18*, 100242. [CrossRef]
35. Bonu, V.; Srinivas, G.; Praveen Kumar, V.; Joseph, A.; Narayana, C.; Barshilia, H.C. Temperature dependent erosion and Raman analyses of arc-deposited H free thick DLC coating on Cr/CrN coated plasma nitrided steel. *Surf. Coat. Technol.* **2022**, *436*, 128308. [CrossRef]
36. Cao, X.; Xiao, R.; Jia, J.; Chen, H.; Dai, E. Fabrication and Tribological Properties of Ni60 Matrix Solid-Lubricating Composites over a Broad Temperature Range. *Coatings* **2022**, *16*, 1345.
37. Cavaleiro, A.J.; Ramos, A.S.; Martins, R.M.S.; Fernandes, F.M.B.; Morgiel, J.; Baehtz, C.; Vieira, M.T. Phase transformations in Ni/Ti multilayers investigated by synchrotron radiation-based x-ray diffraction. *J. Alloys Compd.* **2015**, *646*, 1165–1171. [CrossRef]
38. Daram, P.; Hiroto, T.; Watanabe, M. Microstructure and phase evolution of functionally graded multi-materials of Ni–Ti alloy fabricated by laser powder bed fusion process. *J. Mater. Res. Technol.* **2023**, *23*, 5559–5572. [CrossRef]
39. Chu, J.P.; Lai, Y.W.; Lin, T.N.; Wang, S.F. Deposition and characterization of TiNi-base thin films by sputtering. *Mater. Sci. Eng. A* **2000**, *277*, 11–17. [CrossRef]
40. Feng, Z.-H.; Sun, X.-Y.; Han, P.-B.; Fu, H.; Dong, H.-C.; Guo, S.; Su, R.; Li, J.-H. Microstructure and microhardness of a novel TiZrAlV alloy by laser gas nitriding at different laser powers. *Rare Met.* **2020**, *39*, 270–278. [CrossRef]
41. Zhang, Q.Y.; Zhou, Y.; Wang, L.; Cui, X.H.; Wang, S.Q. Investigation on tribo-layers and their function of a titanium alloy during dry sliding. *Tribol. Int.* **2016**, *94*, 541–549. [CrossRef]

42. Huang, T.-C.; Hsu, S.-Y.; Lai, Y.-T.; Tsai, S.-Y.; Duh, J.-G. Effect of NiTi metallic layer thickness on scratch resistance and wear behavior of high entropy alloy (CrAlNbSiV) nitride coating. *Surf. Coat. Technol.* **2021**, *425*, 127713. [CrossRef]
43. Yang, R.; Li, F.; Huang, Z.; Wang, X.; Yang, H.; Qiao, J. Tribological behavior of MP159 superalloys before and after plasma nitriding at different temperatures. *Tribol. Int.* **2025**, *209*, 110681. [CrossRef]
44. Tian, H.; Xin, J.; Li, Y.; Wang, X.; Cui, Z. Combined effect of cathodic potential and sulfur species on calcareous deposition, hydrogen permeation, and hydrogen embrittlement of a low carbon bainite steel in artificial seawater. *Corros. Sci.* **2019**, *158*, 108089. [CrossRef]
45. Yang, J.; Lu, Y.; Guo, Z.; Gu, J.; Gu, C. Corrosion behaviour of a quenched and partitioned medium carbon steel in 3.5wt.% NaCl solution. *Corros. Sci.* **2018**, *130*, 64–75. [CrossRef]
46. Borowski, T.; Kulikowski, K.; Adamczyk-Cieślak, B.; Rożniatowski, K.; Spychalski, M.; Tarnowski, M. Influence of nitrided and nitrocarburised layers on the functional properties of nitrogen-doped soft carbon-based coatings deposited on 316L steel under DC glow-discharge conditions. *Surf. Coat. Technol.* **2020**, *392*, 125705. [CrossRef]
47. García-León, R.A.; Martínez-Trinidad, J.; Zepeda-Bautista, R.; Campos-Silva, I.; Guevara-Morales, A.; Martínez-Londoño, J.; Barbosa-Saldaña, J. Dry sliding wear test on borided AISI 316L stainless steel under ball-on-flat configuration: A statistical analysis. *Tribol. Int.* **2021**, *157*, 106885. [CrossRef]
48. Kikuchi, S.; Ueno, A.; Akebono, H. Combined effects of low temperature nitriding and cold rolling on fatigue properties of commercially pure titanium. *Int. J. Fatigue* **2020**, *139*, 105772. [CrossRef]
49. Wang, C.; Hong, J.; Cui, M.; Huang, H.; Zhang, L.; Yan, J. The effects of simultaneous laser nitriding and texturing on surface hardness and tribological properties of Ti6Al4V. *Surf. Coat. Technol.* **2022**, *437*, 128358. [CrossRef]
50. Ohtsu, N.; Endo, R.; Takeda, S.; Sakuraba, Y.; Hirano, M. Open-atmosphere laser nitriding of austenitic steels to form wear-resistant surfaces. *Surf. Coat. Technol.* **2024**, *476*, 130275. [CrossRef]
51. Cisquini, P.; Ramos, S.V.; Lins, V.F.C.; Franco, A.R.; Vieira, E.A. Micro-abrasive wear resistance of the duplex expanded austenite layer phases produced by plasma nitrocarburizing. *Wear* **2019**, *436*, 203039. [CrossRef]

Disclaimer/Publisher's Note: The statements, opinions and data contained in all publications are solely those of the individual author(s) and contributor(s) and not of MDPI and/or the editor(s). MDPI and/or the editor(s) disclaim responsibility for any injury to people or property resulting from any ideas, methods, instructions or products referred to in the content.